This is the peer reviewed version of the following article: Spectroscopic insight into the interplay between structural disorder and oxidation degree in melt-grown $Ce_{0.5}Zr_{0.5}O_{2-y}$ compounds, J. Raman Spectrosc. (2020), P.B. Oliete, A. Orera, M. L. Sanjuán, which has been published in final form at DOI:10.1002/jrs.5797.

Spectroscopic insight into the interplay between structural disorder and oxidation degree in melt-grown $Ce_{0.5}Zr_{0.5}O_{2-y}$ compounds

Patricia B. Oliete, Alodia Orera, María Luisa Sanjuán*

Instituto de Ciencia de Materiales de Aragón (Universidad de Zaragoza-CSIC), Facultad de Ciencias, Universidad de Zaragoza, Pza San Francisco s/n, 50009 Zaragoza, Spain

*Corresponding author.

E-mail address: sanjuan@unizar.es

Abstract

The oxygen storage capacity of $Ce_xZr_{1-x}O_{2-y}$ compounds arises from the mixed-valent character of cerium, which makes the system sensitive to external factors such as temperature and oxygen partial pressure through their influence in the Ce valence, cation ordering and oxygen content. In this work we analyze the phase relations in $Ce_{0.5}Zr_{0.5}O_{2-y}$ compounds fabricated by the laser floating zone (LFZ) technique in either oxidising or reducing atmosphere. Chemical, structural and microstructural properties are studied by XRD, TG, SEM (EDX, EBSD) and Raman spectroscopy. The latter proves to be determinant to discriminate between phases arising from subtle variations of atomic distribution that are hardly distinguished by XRD or EDX analyses. Cation disordered, fluorite-like phases are obtained when processing is performed in air whereas cation-ordered, pyrochlore-related phases are formed when processing in Ar+5%H_2 atmosphere. Processing in a low but non -negligible pO_2 yields, besides the pyrochlore and fluorite-like phases, an intermediate state with partial disorder that may be relevant for catalysis applications. The vibrational Raman spectrum of the $Ce_2Zr_2O_7$ pyrochlore has been fully interpreted through polarisation measurements at room and low temperature. Bands arising from crystal field transitions within the ground and first excited multiplets of Ce^{3+} ions are also identified. The electronic Raman spectrum is found to be a sensitive probe of the degree of cation and oxygen order in these compounds.

KEYWORDS: CeO_2-ZrO_2, Raman, $Ce_2Zr_2O_7$ pyrochlore, order-disorder, redox

1| INTRODUCTION

Among the many applications of Ce-based oxides in the catalysis field, their use as oxygen storage compounds (OSC) in three-way-catalyst supports is among the most successful ones (see Refs. [1,2,3] and references therein). This application takes advantage of the ability of cerium compounds to take up or release oxygen through the redox reaction

$$2Ce^{4+} + O_O^x \rightleftarrows 2Ce^{3+} + \tfrac{1}{2}O_2(g) + V_O^{\bullet\bullet} \qquad (1)$$

It was soon discovered that the addition of Zr to CeO_2 is beneficial for the OSC properties, both because it provides a higher stability against grain growth and also because it lowers the temperature of the first peak in temperature programmed reduction (TPR) experiments.[4]

The OSC properties of $Ce_xZr_{1-x}O_{2-y}$ (CZO) compounds depend mainly on three variables: i) cation stoichiometry; ii) cation distribution (order/disorder phenomena involved) and iii) Ce redox state and oxygen content.

There is now consensus in that the best OSC behaviour is found for Ce contents $x \approx$ 0.5-0.6.[4] The variation of the OSC properties with the Ce concentration and their optimization for intermediate Ce content have been related to the ability of Zr and Ce ions to adopt an ordered pyrochlore-type configuration, which seems to ease both the ionic and electronic conduction processes involved in the redox reaction.[5]

It is clear that in this context the knowledge of the phase relations from reduced to oxidised states, or from ordered to disordered phases, is of paramount importance. Many studies have been performed to understand the behaviour of CZO materials upon variation of the temperature and atmosphere of thermal treatments.

Although it is common to discuss the properties of the CZO systems in terms of the ZrO_2-CeO_2 phase diagram (PD),[6] this is strictly valid only for oxidising conditions. To account for Ce reduction, the ZrO_2-Ce_2O_3 PD[7] should be used instead; however weak reduction effects can be

handled by drawing in the ZrO_2-CeO_2 PD additional lines that represent metastable phases.[8] For instance, despite there are no stable phases with intermediate Ce/Zr composition in the ZrO_2-CeO_2 PD, a metastable, cation-disordered $Ce_{0.5}Zr_{0.5}O_2$ tetragonal phase (*t*') can be formed by fast cooling from temperatures above ~1600 °C in air, followed by mild reoxidation below 600 °C.[8,9] In strongly reducing conditions the larger size of Ce^{3+} leads to cation ordering in the stable $Ce_2Zr_2O_7$ pyrochlore (*p*) phase.[7] Subsequent oxidation of *p*-$Ce_2Zr_2O_7$ at moderate temperatures will yield metastable $Ce_2Zr_2O_{7+z}$ phases up to the fully oxidised $Ce_2Zr_2O_8$ κ-phase described in Ref. [10]. To make clear whether we deal with ordered or disordered phases we shall write $Ce_{0.5}Zr_{0.5}O_{2-y}$ for fluorite-like, cation disordered phases and $Ce_2Zr_2O_{7+z}$ for pyrochlore-like, cation-ordered phases. Note that *y* and *z* in these formulae are only expressing a possible stoichiometry deviation from fully oxidised or fully reduced fluorite or pyrochlore phases, respectively.

Phases formed for intermediate reduction degree are still not well known. The existence of a $Ce_2Zr_2O_{7.5}$ phase with $F\bar{4}3m$ space group (SG), midway between pyrochlore ($Fd\bar{3}m$ SG) and κ-phase ($P2_13$ SG), was reported by Sasaki et al.[11] and labelled as "β-phase". Both in that work and in the subsequent study by Achary et al.[12] the intermediate phase was ascribed to the half filling of the pyrochlore anionic vacancies. The path from the reduced to the oxidised compounds and vice-versa at moderate temperatures is known (DF to *t*', *p* to κ) but the problem acquires higher complexity when high temperature processes are added to the equation, since the activation of cation diffusion may result in a change of the ordered or disordered character of the compound. Despite their presumable relevance in practical applications, states with intermediate order degree are still relatively unexplored, although they may be the key to understand the complex TPR results of catalysts characterisation, where reduction temperatures close to 1000 °C are employed.[5]

The Ce valence in cerium oxides is a function of oxygen partial pressure and temperature, so that at high temperatures Ce tends to become reduced even in an oxidising atmosphere,[13,14] a fact that has to be taken into account when performing oxidising treatments at high temperatures. In this work we approach the problem by producing crystalline materials by laser assisted directional solidification, denoted as LFZ (laser floating zone), in which melting is achieved by heating the sample with the help of a high power CO_2 laser with no need of a crucible. In the context of the CZO system, the LFZ technique is interesting because it allows reaching very high temperatures (above 2500 °C if required) that open a range of reduction possibilities difficult to attain by conventional solid-state reaction. Moreover, the kinetics of LFZ processing allows investigating far from equilibrium situations, which are relevant in the complex CeO_2-Ce_2O_3-ZrO_2 system, and variation of the processing atmosphere between oxidising and reducing conditions enriches the possibilities of attainable phases.

One of the purposes of this work is to take benefit of all these characteristics to explore the interplay between order/disorder phenomena and the oxidation state in CZO compounds.

The availability of single crystalline samples enables precise Raman spectroscopic measurements, which is mandatory for an accurate interpretation of the spectra and their further use to investigate the variations in the atomic distribution. We finally point that obtaining large single-crystalline grains prevents fast oxidation of the $Ce_2Zr_2O_7$ pyrochlore phase which, in polycrystalline form, readily oxidises to $Ce_2Zr_2O_{7+z}$ after exposure to air even at RT.[15]

Raman scattering is widely used in the study of CZO materials because of its sensitivity to small variations of the oxygen atomic distribution that result in phases with almost indistinguishable XRD patterns. The ability to detect local disorder and size effects is in fact one of the strengths of Raman scattering.[16] In the context of laser-processed materials, the analysis of the spatial distribution of the spectra through Raman mapping has proven to be essential in this work in

the discussion of the oxygen and cation diffusion mechanisms. Traditional techniques, such as XRD, give only average sample composition so that information on the spatial phase distribution is lost.

A detailed Raman spectroscopic investigation of the $Ce_2Zr_2O_7$ pyrochlore has also been performed. Polarisation measurements at low temperature (77 K) have enabled the identification of electronic Raman transitions between crystal field split levels of Ce^{3+} not hitherto studied. Although far from the scope of this work, we note that $Ce_2Zr_2O_7$ has received interest in recent times because of its magnetic properties as a "quantum spin ice" or "quantum spin liquid",[17,18] so that providing an accurate analysis of vibrational, electronic and mixed character excitations may contribute to a deeper understanding of the physical properties of this compound at low temperatures.

2| EXPERIMENTAL DETAILS

Rods of nominally $Ce_{0.5}Zr_{0.5}O_2$ composition were directionally solidified using the LFZ method. Ceramic precursors were prepared by solid state reaction using a mixture of commercial powders of CeO_2 (Aldrich, 99.9%) and m- ZrO_2 (Aldrich, 99%) with the 50/50 molar composition. Cylindrical precursors were fabricated by isostatically pressing the powder for 3 min at 200 MPa and sintering at 1500 °C either during 12 h in air. To verify the possible influence of the oxygen content of the precursor in the properties of the processed material, some experiments were made with precursors sintered in Ar + 5%H_2, but the resulting phase content and microstructure were found to be independent of the oxygen stoichiometry of the precursor. In this work we shall only present results of samples processed from air-sintered precursors. Rods were processed using 80-100 W of a CO_2 laser (λ= 10.6 μm) as heating source, either in air or in Ar + 5%H_2 atmosphere with 0.1-0.2 bar overpressure with respect to

ambient pressure. The processing rate was varied between 100 and 750 mm/h to test the influence of solidification rate in phase homogeneity and stoichiometry. Growth at 100 mm/h resulted in significant CeO_2 evaporation and those experiments will not be presented here. The best results were obtained for growth rates above 300 mm/h. The final diameter of the solidified rods was between 1.4 and 2.0 mm.

Transverse and longitudinal cross-sections of the rods were cut and polished for scanning electron microscopy (SEM) and Raman analysis. The microstructure was studied using the back-scattered and secondary electron images obtained in a Field Emission SEM (model Carl Zeiss MERLIN). Crystal grain orientation was analysed in the same microscope with an integrated EBSD system from Oxford Instruments. Chemical analysis was performed by energy dispersive X-ray spectroscopy (EDX).

X-ray diffraction (XRD) experiments were carried out on a Rigaku D/max 2500 diffractometer with Cu Kα radiation working at 40 kV and 100 mA. Data were collected in a step mode ($\Delta 2\theta$ = 0.03°) and a counting time of 3s per step. Thermogravimetric analyses (TGA) were carried out in a Q600 thermobalance of TA Instruments, with a heating rate of 10 °C/min under flowing air. ~25 mg of crushed samples were used in these experiments.

Raman spectroscopy was performed using a DILOR XY spectrometer with a CCD detector and 2 cm^{-1} of spectral resolution. The 514.5, 496.5 and 488 nm lines of an Ar^+-ion laser and the 647 nm line of a Kr^+ laser were used as excitation sources. The power at the sample surface was <20 mW. This power was found to be a safe limit below which heating effects, if present, did not affect the spectra. A 50X microscope objective lens of an Olympus BH-2 microscope was used both for excitation and dispersed light collection, providing a lateral spatial resolution of 2 μm. The same microscope was used to record optical images of the samples, in this case with a 5X objective lens. Low temperature measurements were performed in a SMC-TBT liquid-nitrogen-cooled cryostat.

3| EXPERIMENTAL RESULTS

To test the influence of the processing atmosphere in the phase content of the resulting material, samples were processed at different oxygen partial pressure of the LFZ chamber. Sample ALFZ was processed in air, sample HLFZ was processed in Ar + 5% H_2, and sample PLFZ was processed in an intermediate oxygen partial pressure $P_{O2} \simeq 0.01$ bar.

3.1| Processing in air (ALFZ sample)

Fig. 1(a) shows a secondary electron image of a transverse section of the 1.8 mm diameter rod processed in air at 300 mm/h. It shows a quite homogeneous macroscopic aspect, though some cracks are visible.

A portion of the rod was crushed and analysed by XRD. The pattern (see Fig. 2(a)) is characteristic of a fluorite phase with a = 5.2734(1) Å, though some very weak peaks at the high angle side of the main peaks denote the presence of a low amount of a second phase, which was identified by Raman measurements as a tetragonal t'-like phase. Introducing that phase in the XRD fit yielded $a_{t'}$ = 3.7080(1) Å and $c_{t'}$ = 5.2939(2) Å (see fit in Fig. S1 (Supporting Information)). Both lattice parameters are below those of t'-$Ce_{0.5}Zr_{0.5}O_2$ (a = 3.7222(1) Å, c = 5.3109(1) Å),[19] implying a lower Ce content in the processed rod. This hypothesis was confirmed by Raman measurements recorded radially on the transverse section (Fig. 1(b)), which showed a homogenous defect-fluorite-like spectrum throughout the sample with the exception of a narrow ring close to the rod surface, ~ 30 μm wide, where t'-like spectra were found. The t' spectrum at the surface is close to that of the t'-$Ce_{0.4}Zr_{0.6}O_2$ processed material[20] thus confirming that some Ce loss has been produced by volatilisation during melting.

The stoichiometry of the defective cubic phase could not be elucidated from Raman measurements alone but the black colour of the sample indicated that some reduction was

occurring, despite the oxidising atmosphere. Partial Ce reduction was confirmed by the detection of the electronic Raman transition between the $^2F_{5/2}$ and $^2F_{7/2}$ multiplets of Ce^{3+} around 2100 cm^{-1} (see inset in Fig. 1(b)).[21] On the other hand, the presence at the sample edge of a *t*'-like spectrum, typical of highly oxidised compounds, suggests that oxidation is taking place at the sample surface in contact with the air atmosphere of the chamber. Allowing for the likely Ce loss, the stoichiometry of this sample is written as $Ce_{0.5-\varepsilon}Zr_{0.5+\varepsilon}O_{2-y}$, *y* being higher at the rod centre than at the surface.

With the aim of determining more accurately the effect of cerium evaporation, the spatial distribution of the chemical composition was analysed by EDX (see Fig. S2 (Supporting Information)). The relative Ce content varied from 0.47 ± 0.01 at. per formula unit (pfu) at the centre to 0.46 ± 0.01 at. pfu at the edge with a minimum of 0.44 ± 0.01 at. pfu at 200 μm from the surface. EDX then confirms the lower-than-nominal Ce content suggested by XRD and Raman data. Absolute oxygen content could not be properly analysed, but was found roughly constant throughout the whole section, as shown in Fig. S2 (Supporting Information).

The average oxygen content per formula of the ALFZ processed rod was derived from TG experiments in air up to 800 °C, which showed a gain of ≈ 0.35% weight (see Fig. S3(a) (Supporting Information)). Taking from EDX a mean $Ce_{0.45}Zr_{0.55}$ cation composition and assuming a fully oxidised state after the TG run the final composition would be $Ce_{0.45}Zr_{0.55}O_2$, from which we derive an initial average composition of $Ce_{0.45}Zr_{0.55}O_{1.97}$. After the TG run the ALFZ sample had converted into a single *t*'-phase (see Raman spectra in Fig. S4 (Supporting Information)).

3.2| Processing in Ar + 5% H_2 (HLFZ sample)

Fig. 3 shows a secondary electron image of the transverse section of the ~1.5 mm diameter rod grown in Ar + 5%H_2 atmosphere at 300 mm/h. The aspect is quite homogeneous although a different texture is seen near the surface, forming an outer region ~70 μm wide. The central

area is formed by square-like grains. Their orientation has been analysed by EBSD, presented in the Supporting Information, which shows that the normal direction is close to a <001> axis.

EDX analysis showed that the cerium content is basically constant along the whole sample radius, within experimental error, and that Ce/Zr ≃1 (see Fig. S5 (Supporting Information)). It is interesting that cerium evaporation seems to be lower when processing in Ar + 5% H_2 than when processing in air. This difference may be attributed to the gas overpressure used in the growth chamber when processing in Ar + 5% H_2 atmosphere.

The XRD pattern of this sample is shown in Fig. 2(b). It displays a basically cubic fluorite pattern with superstructure peaks characteristic of a pyrochlore-like cation ordering. A rough fit of this pattern with a single pyrochlore phase gives a ~10.7 Å. However, a close look at the high angle peaks (see inset) evidences the presence of weak shoulders indicating a more complex phase content. We note that all the peaks display the same behaviour, which suggests a splitting between at least two different cation-ordered phases with slightly different lattice parameters, thus with different reduction degree. A much more precise picture of phase content and spatial distribution is achieved by Raman mapping performed onto a transverse section.

The right part of Fig. 3 shows representative Raman spectra recorded on the HLFZ sample. At the rod centre, covering the central region up to a distance of ~100 μm from the surface, the spectrum labelled (a) in Fig. 3 was systematically found. The band positions and relative intensities of this spectrum are similar to those of pyrochlore $Ce_2Zr_2O_7$ reported by Omata et al.[10] and Kasano et al.[22] Spectrum (a) is also closely related to those of other $R_2Zr_2O_7$ pyrochlores in which *R* is a large rare earth element such as La, Pr or Nd.[23,24]

We therefore assign spectrum 3(a) to the $Ce_2Zr_2O_7$ pyrochlore phase. At this point we mention that there is still some ambiguity in the literature concerning the Raman spectrum of $Ce_2Zr_2O_7$. Whereas Omata et al.[10] and Kasano et al.[22] report spectra similar to ours, Urban et al.[15] assign a different spectrum to the pyrochlore phase although they precise that the

composition of their sample is $Ce_2Zr_2O_{7.3}$. In fact, the spectrum reported in Ref. [15] is very similar to spectrum 3(c). We shall return to this point later on. Since Kasano et al. and Omata et al. do not perform a band assignment, and because of some confusion about the band symmetry in $R_2Zr_2O_7$ pyrochlores, we have performed a detailed Raman study of the $Ce_2Zr_2O_7$ pyrochlore taking benefit of the availability of our LFZ-processed crystalline samples. The remarkable quality of the pyrochlore phase obtained with this technique offers also an opportunity to discuss the origin of some ambiguous bands in this and other pyrochlores. This study is presented in section 3.4.

Spectrum 3(b) was still found in the inner part of the transverse section but closer to the rod surface. It presents common features with the pyrochlore spectrum but its weaker intensity (note the $\times$ 0.2 factor of spectrum 3(a)) and broad aspect suggest some kind of structural disorder. At this point, it is very interesting to note that spectrum 3(b) presents, besides the usual pyrochlore bands, an additional band around 600 cm^{-1} with medium intensity, which has sometimes been assigned to a T_{2g} mode.[23,24] Bands in $R_2Zr_2O_7$ pyrochlores around this wavenumber usually denote oxygen disorder and are increasingly activated as R becomes smaller, due to the creation of cation antisite defects and anion vacancy occupation. In our case, the appearance of such a band can be attributed to the presence of a small concentration of Ce^{4+} ions. The excess positive charge would be compensated by extra oxygen anions occupying the vacant site, resulting in the activation of formally forbidden Zr-O modes. We therefore attribute spectrum 3(b) to a slightly oxidised $Ce_2Zr_2O_{7+z}$ phase preserving cation order but with additional oxygen population at the vacant sites.

Now we discuss on spectrum 3(c). As we have said, a very similar spectrum was attributed in Ref. [15] to a pyrochlore phase with $Ce_2Zr_2O_{7.3}$ stoichiometry but the clearly distinct aspect from the pyrochlore spectrum suggests a substantially different atomic distribution. To clarify this point, we have produced $Ce_2Zr_2O_{7+z}$ samples with $z \simeq 0.3$ and 0.5 (labelled as N7.3 and

N7.5 for short) by solid-state reaction at 1500 °C in a reducing atmosphere. The furnace pO_2 was varied to get samples with different oxygen content.

The XRD patterns and Raman spectra of these compounds are presented in Fig. 4. It is clear that the Raman spectrum of sample N7.3 is similar to that of Fig. 3(c), wavenumber differences being smaller than 3 cm^{-1}. Both N7.3 and N7.5 compounds display cubic pyrochlore-like XRD patterns with lattice parameters a = 10.655(1) Å and a = 10.646(1) Å for N7.3 and N7.5, respectively, which are significantly smaller than that of the $Ce_2Zr_2O_7$ pyrochlore phase (a = 10.7414(3) Å[10]), in agreement with partial oxidation. The lattice parameter of N7.3 is very similar to that reported for the $Ce_2Zr_2O_{7.3}$ compound in Ref. [15], whereas the lattice parameter of N7.5 is close to that of the compound $Ce_2Zr_2O_{7.5}$ with $F\bar{4}3m$ SG named β-phase in Ref. [11]. A distinctive feature of the β-phase is a weak peak at the angle (~16.7°) corresponding to the (200) reflection, which is allowed in the $F\bar{4}3m$ SG but forbidden in the pyrochlore $Fd\bar{3}m$ SG. A close look at the XRD patterns of N7.3 and N7.5 samples (see inset in Fig. 4), evidences that both samples present weak peaks at this position (more intense for N7.5, as expected), implying that they are better described as β-phases than as pyrochlore ones. We then attribute the Raman spectra of the N7.3 sample and in consequence spectrum 3(c) to a β phase with $Ce_2Zr_2O_{7.3}$ composition. The preceding results extend the existence domain of the β-phase to lower oxygen content, at least to 7.3 atoms per pyrochlore formula unit.

Summing up, Raman mapping provides an explanation for the XRD peak splitting as due to the coexistence of cation ordered phases with different oxygen content, evolving from the main, almost stoichiometric $Ce_2Zr_2O_7$ phase, toward a β phase with ~ $Ce_2Zr_2O_{7.3}$ composition. In an attempt to explain the XRD pattern, we have introduced three cation-ordered phases in the fitting procedure, which yields $a_1 \simeq$ 10.727 Å, $a_2 \simeq$ 10.693 Å and $a_3 \simeq$ 10.646 Å (see Fig. S6 (Supporting Information)). The first lattice parameter is in good agreement with that of the

pyrochlore phase, whereas the last one belongs to the β-phase with the proposed composition. The second one accounts for the presence of slightly oxidised pyrochlore regions. The low phase percentage of the oxidised pyrochlore and β phases and their close lattice parameters make it impossible to identify the nature of these phases exclusively by XRD.

The TG mass gain of the HLFZ sample (Fig. S3(b) (Supporting Information) is close to 2 %, from which an average initial stoichiometry $Ce_2Zr_2O_{7.28}$ is derived. In agreement with the fully ordered character of this sample, after the TG it transforms into a single κ-phase (see Fig. S7 (Supporting Information)).

3.3| Processing in intermediate pO_2 (PLFZ sample)

Fig. 5 shows an optical image of a transverse cut of the PLFZ sample. It presents a more or less circular crack separating an inner core from an outer shell ~250 μm wide. Radial cracks are also found, especially in the outer region. The magnification of the inner part (see Fig. S8 (Supporting Information)) shows that, in contrast with the square-like grains in the HLFZ sample, here the grains have and irregular, quasi-hexagonal shape. Their orientation has been analysed by EBSD (see the Supporting Information); the plane normal is a [11z] direction intermediate between [110] and [111] axes.

A portion of the sample was crushed and analysed by XRD. Its pattern, shown in Fig. 2(c), shows that all fluorite-like peaks are doubled, which suggests the presence of at least two cubic phases with substantially different lattice parameter, roughly $a_1 \simeq 10.67$ Å and $a_2 \simeq 10.55$ Å. According to the difference in ionic radii of Ce^{3+} and Ce^{4+} ions, low angle components should belong to more reduced phases and high angle components to more oxidised ones. Peaks denoting pyrochlore-like superstructure are also doubled (see inset in Fig. 2), implying that both phases present some degree of cation ordering. However, it has to be noted that the

relative intensities of the superstructure peaks are different from those of the main peaks: the low angle superstructure peaks are always more intense than the high angle ones, whereas the relative intensities are more similar for the main fluorite-like peaks. Based on the Raman results to be presented later on, we attribute this fact to the coexistence of at least two oxidised phases with different ordering degree, only the ordered ones contributing to the superstructure peaks.

Elemental content was studied by EDX. As Fig. S9 (Supporting Information) shows, there is a discontinuity in the oxygen content between the inner and the outer regions, being higher near the rod surface than at the centre. As regards the Ce concentration, it is close to 50% of the total cation content in the rod core up to $\sim$ 300 μm from the surface, and then slightly decreases down to 49% at the sample edge.

Raman mapping was undertaken over regions from the centre to the edge of the rod. A reproducible sequence of spectra was found throughout the sample when measurements were collected radially, as shown in the right part of Fig. 5. Differences were attributed to phases with varying degree of cation order and oxygen content. Note that, as crystallization occurs at very high temperatures, the sequence of spectra shown in Fig. 5 represents the path of simultaneously increasing oxidation *and* cation disorder.

3.3.1| Phase assignment in the PLFZ sample from Raman results

At the rod centre, and covering the homogeneous region inside the outer ring, the spectrum labelled as (a) in Fig. 5 was systematically found. It resembles closely that of Fig. 3(b) that we have attributed to a slightly oxidised pyrochlore phase, and is in agreement with the XRD detection of a phase with $a \simeq 10.67$ Å, which is below but close to the lattice parameter of the $Ce_2Zr_2O_7$ pyrochlore.[10,12] In spectrum 5(b) we recognise a spectrum similar to that of Fig. 3(c)

that we have assigned to the β-phase with composition $\simeq Ce_2Zr_2O_{7.3}$. Spectrum β was found in intermediate regions between the inner part and the outer ring. Despite the close similarity between the XRD patterns of pyrochlore and β-phases,[12] there is not a soft evolution from the pyrochlore to the β spectrum, implying that the extra oxygen atoms of the β phase force a significant displacement of the oxygen coordinates that has a pronounced effect in the Raman spectrum.

Spectra 5(d) and 5(e) from the outer area are attributed to cation-disordered phases with high oxygen content. Spectrum (e) is characteristic of a highly oxidised tetragonal *t'*-$Ce_xZr_{1-x}O_2$ phase with $0.45 \leq x \leq 0.5$.[20] Spectrum 5(d), in turn, is very similar to that found in the ALFZ sample, where the phase content was mainly a cubic DF phase.

The most interesting aspect of Fig. 5 is the appearance of a *transition* spectrum (5(c)) between the β and DF or *t'* regions. It resembles spectra reported in the literature for $Ce_{0.5}Zr_{0.5}O_2$ compounds submitted to reduction treatments in the temperature range of 1050 - 1100 °C followed by mild reoxidation[10,25,26] and assigned to κ-phases with some undetermined variation of the anion distribution[26] or to the occurrence of cation disorder resulting in antiphase-boundaries.[10] The assignment in those works was based on the persistence in XRD of some superstructure peaks denoting cation ordering, despite the loss of the weak reflections characteristic of the $P2_13$ SG of the κ-phase. We think that the disappearance of those peaks and the appreciable difference between the Raman spectrum 5(c) and that of the κ-phase[10] deserve considering this phase as different from κ-$Ce_2Zr_2O_8$. The localization of spectrum 5(c) close to the crack separating reduced/ordered from oxidised/disordered phases suggests that it corresponds to a state with intermediate degree of both reduction *and* cation ordering. Partial reduction is supported by the detection of the Ce^{3+} electronic Raman spectrum in regions displaying spectrum 5(c) (see section 3.4.1). However, spectrum 5(c) is preserved after full oxidation in TG experiments up to 800 °C (see Fig. S10 (Supporting

Information)), implying that the main difference with the κ–phase arises from incomplete cation order, with or without oxygen deficiency. This also agrees with its formation at temperatures just at the onset of cation redistribution. We shall denote as δ the CZO state yielding spectrum 5(c). Note that the spectra reported in Refs. [10,25] belong to fully oxidised samples whereas we here show that the domain-like phase appears in reducing conditions and is preserved after oxidation.

The TGA curve of the PLFZ sample (Fig. S3(c) (Supporting Information)) shows a mass gain of $\simeq$ 1.2 %, which implies an average initial composition of $Ce_2Zr_2O_{7.56}$. As shown in Fig. S10 (Supporting Information), after the TG run Raman scattering evidences the presence of κ, t' and δ-phases, coming from the cation ordered, disordered and intermediate regions, respectively.

3.4| The Raman spectrum of $Ce_2Zr_2O_7$: phonons and crystal field transitions

Polarised Raman spectra of pyrochlore $Ce_2Zr_2O_7$ were recorded onto (001) oriented crystalline grains identified in the transverse section of the HLFZ sample by rotating the sample around the perpendicular direction. The 90° spectrum periodicity confirmed the (001) surface orientation where we identified directions compatible with [100] and [110] crystal axes.

The left part of Fig. 6 depicts spectra recorded at RT in *z*(*xx*)-*z* , *z*(*xy*)-*z* , *z*(*x'x'*)-*z* and *z*(*x'y'*)-*z* configurations, were the usual Porto's notation ***k***($\alpha\beta$)***k'*** is used. The light propagation directions ***k***, ***k'*** will be omitted for short, so that spectra will be labelled by the directions of the incident and scattered electric field polarisation directions α,β.

According to the crystal symmetry and site occupancies, the phononic Raman activity for $A_2B_2O_7$ pyrochlores with $Fd\bar{3}m$ SG is A_{1g} + E_g + 4T_{2g}.[27] Because *A* and *B* cations occupy

inversion symmetry sites, all Raman modes involve exclusively the vibration of oxygen atoms. The Raman tensors appropriate to the O_h symmetry are

$$A_{1g} = \begin{pmatrix} a & & \\ & a & \\ & & a \end{pmatrix};\ E_g = \begin{pmatrix} b & & \\ & -b & \\ & & \end{pmatrix}, \frac{1}{\sqrt{3}}\begin{pmatrix} b & & \\ & b & \\ & & -2b \end{pmatrix};$$

$$T_{2g} = \begin{pmatrix} & & d \\ & d & \\ d & & \end{pmatrix}, \begin{pmatrix} & & d \\ & & \\ d & & \end{pmatrix}, \begin{pmatrix} & d & \\ d & & \\ & & \end{pmatrix},$$

from which the expected Raman activity is A_{1g} (a^2) + E_g ($4b^2/3$) in xx; T_{2g} (d^2) in xy; A_{1g} (a^2) + E_g ($b^2/3$) + T_{2g} (d^2) in $x'x'$ and E_g (b^2) in $x'y'$. We readily identify the A_{1g} mode at 497 cm^{-1}, the E_g mode at 300 cm^{-1} and two T_{2g} modes at 294 and 392 cm^{-1}, respectively. Note that the overlapping T_{2g} and E_g modes around 300 cm^{-1} has been resolved, for the first time to our knowledge, thanks to the availability of large crystals for polarization measurements. These values can be compared with those calculated by Nandi et al.[28] for $R_2Zr_2O_7$ pyrochlores with R = La, Nd, Sm and Eu: 516 - 529 cm^{-1} for the A_{1g} mode, 335 - 354 cm^{-1} for the E_g mode, and in the ranges 290 – 298 and 376 – 391 cm^{-1} for the first two T_{2g} modes. We thus see that our experimental values are in general lower than the calculated ones.

The other two T_{2g} modes are predicted around 460 - 472 and 575 - 587 cm^{-1} for R = La, Nd in Ref. [28]. As regards the latter mode, although a weak feature is seen in the xx and $x'x'$ spectra of $Ce_2Zr_2O_7$ around 587 cm^{-1}, its polarisation properties do not agree with the expectations for a T_{2g} mode; it rather behaves as an A_{1g} mode. We note that pyrochlores are highly anharmonic lattices[29] and that this favours the enhancement of second-order features, especially in the A_{1g} channel. Alternatively, the band at 587 cm^{-1} might be due to a low amount of extra oxygen atoms at the vacancy site (see the discussion about this point in section 3.2). On the other hand, there is another weak band, at 527 cm^{-1} at RT, which has much closer T_{2g} character (see inset in Fig. 6). We tentatively assign it to the third T_{2g} mode.

The fourth T_{2g} mode has been assigned as follows: A broad band with remarkable intensity appears around 448 cm^{-1} at RT, a position that fits well with the value predicted in Ref. [28]. However, the band does not fulfil polarisation rules for a T_{2g} mode. In a remarkable coincidence, a crystal field (CF) transition within the $^2F_{5/2}$ ground state multiplet of Ce^{3+} has been found by inelastic neutron scattering (INS) at the very same energy.[17,18] It is strongly appealing to see whether the two kinds of excitations are superposed in Raman spectra and whether they can be resolved in low temperature measurements. *xx* and *xy* spectra recorded at 77K, shown in the right part of Fig. 6, unambiguously solve the question and confirm that there are two different excitations at very close wavenumbers. From them, the one observed at 446 cm^{-1} in the *xy* spectrum at 77K is assigned to a T_{2g} mode and the one at 455 cm^{-1}, which is observed in all configurations, is attributed to the electronic Raman (ER) excitation within the $^2F_{5/2}$ sublevels also observed in INS. We now discuss with more detail on the electronic Raman spectrum of Ce^{3+} in $Ce_2Zr_2O_7$ and in other CZO phases.

3.4.1| The electronic Raman spectrum of Ce^{3+}

The ground state $^2F_{5/2}$ manifold of Ce^{3+} splits into three Kramers doublets in the D_{3d} local field of the R^{3+} site of the pyrochlore structure. In turn, the first excited multiplet $^2F_{7/2}$ ($E \gtrsim 2100$ cm^{-1}) splits into four doublets.The Raman activity of ER transitions within these levels depends on the ground state symmetry and the multiplication rules $\Gamma_i x \Gamma_j$ between the initial and final states in D_{3d} symmetry but taking into account that measurements are performed along the cubic <100> or <110> axes, not along the Ce^{3+} local ones. After some geometrical calculations we find that all CF transitions are in principle allowed in any geometry, so that we expect CF transitions to appear as non or weakly polarised bands. A detailed calculation of the ER intensities would require the knowledge of the electronic wavefunctions and has not been attempted; we here derive the selection rules based exclusively on the level symmetries.

Refs. [17,18] show that two CF transitions are expected within the $^2F_{5/2}$ manifold, the already mentioned transition at 448 cm^{-1} to the first excited doublet and another one at 880 cm^{-1} to the second excited doublet, in very good agreement with the highest wavenumber band of Fig. 6. However, the Raman spectra show additional broad bands at ~ 810 and 720 cm^{-1}. In fact, similar features were observed by INS in Ref. [18] and attributed to vibronic (phonon + CF transition) combinations. Measurements at 496.5 and 514.5 nm laser wavelengths display the same spectrum, which supports the Raman character of these excitations. However, the bands are strongly depleted when measured at the much longer wavelength of 647 nm. The enhancement of the electronic Raman bands when exciting at 496.5 or 514.5 nm is attributed to a resonance phenomenon occurring on approaching the Ce^{3+} absorption band in the near uv.[21] The wavenumbers of the Raman bands observed below 3000 cm^{-1} and their attribution are collected in Table 1.

Fig. 7 shows spectra in the region of $^2F_{5/2} \rightarrow {}^2F_{7/2}$ intermultiplet transitions of Ce^{3+}. The splitting of the $^2F_{7/2}$ multiplet in trigonal symmetry into four doublets implies that four transitions should be observed, if all of them are Raman active. The spectra displayed in Fig. 7 present three intense, narrow bands and a broad high frequency band, plus additional weaker features in the proximity of the narrow bands. We attribute the main bands to the four expected CF transitions and the weak features either to vibronic coupling or to the presence of a low amount of Ce^{3+} ions in a different configuration, such as antisite defects or with a nearby perturbation.

We have found substantial differences among the ER spectrum of Ce^{3+} in the different CZO phases identified in this work. As Fig. 8 shows, the main band (at 2100-2150 cm^{-1}) is very narrow for the stoichiometric pyrochlore but appears rather broad for all other phases. We also see that it shifts from ~2145 cm^{-1} for *p* and β phases to ~2105 cm^{-1} for DF and *t*' phases, and appears at ~2130 cm^{-1} in the δ-phase, in agreement with its intermediate character

between ordered and disordered phases. Fig. 8 also shows that the high frequency bands disappear dramatically upon introducing some kind of disorder into the pyrochlore lattice, either by increasing oxygen content or in the form of cation disorder. This opens the interesting possibility of using the Ce^{3+} band not only as an evidence of sample reduction but also as an indicator of its ordered or disordered character.

4| DISCUSSION

The preceding results show that the phase content of LFZ-processed CZO rods depends crucially on the processing atmosphere. Processing in air produces only cation-disordered phases, namely a partially reduced defect fluorite as major phase with some *t*' content near the surface. In turn, in Ar + 5% H_2 only cation-ordered *p*-phases are obtained, with a minor amount of the partially oxidised β–phase close to the rod surface. For intermediate pO_2 a two-region separation develops, with ordered and disordered phases appearing at the inner and outer regions of the rod, respectively. The identification of a distinct Raman spectrum around the crack separating these two regions suggests that a *transition* phase exists (labelled δ in this work), involving partial disordering of the cations. This intermediate state between pyrochlore and fluorite-like phases would be analogous to that reported for reduction of *t*'-CZO at moderate temperatures followed by mild reoxidation and attributed to κ-like domains separated by anti-phase boundaries, with the particularity that we find it also in reduced samples.[10]

The instability of $Ce_2Zr_2O_{7+z}$ pyrochlores upon oxidation and the appearance of a domain structure can be related to the evolution of the $R_2Zr_2O_7$ pyrochlores upon decreasing the lanthanide size. The pyrochlore structure is stable if $1.46 \lesssim r \lesssim 1.80$, *r* being the ratio of the R^{3+} and Zr^{4+} ionic radii in VIII and VI coordination, respectively.[30,31] As *r* approaches the lower limit

of 1.46, increasing disorder develops in the form of cation antisite defects and anion-vacancy population, eventually leading to a fluorite phase. Electron diffraction shows that disordered compounds contain *p*-domains surrounded by antiphase boundaries and that domain size decreases on approaching *R*= Gd (*r*=1.46).[32,33] Domains are not observed for La and Nd zirconates. The case of $Ce_2Zr_2O_7$ is particular, because of the possible occurrence of Ce^{4+} together with Ce^{3+}. The large Ce^{3+} ions are unlikely to occupy the octahedral sites, but Ce^{4+} might do, so that an increase of Ce oxidation state favours the stabilisation of a fluorite phase at high temperature.

For low oxidation levels, pyrochlore is the stable form of $Ce_2Zr_2O_{7+z}$, both at low and high temperatures. The situation for intermediate oxidation depends on the temperature at which oxidation events take place. At low temperature, moderate oxidation leads to an oxidised pyrochlore with extra oxygen ions at the anion vacancies, but if temperature is high enough to enable cation mobility, the simultaneous occurrence of cation disorder and oxidation events may lead to a mixed configuration in which large ordered domains, retaining a *p*-like structure and spectrum, coexist with disordered regions. As pO_2 increases the domain size decreases until the *p* spectrum is lost. This is the δ-phase. Finally, in a highly oxidising atmosphere and at high temperatures the DF phase forms with low but non-negligible Ce reduction.

The ensemble of experiments suggests that the final phase content is established at three temperature stages:

1) In the melt state under laser heating the reduction degree is governed by the redox reaction[34]

$$4Ce^{4+}_{(melt)} + 2O^{2-}_{(melt)} \rightleftarrows 4Ce^{3+}_{(melt)} + O_{2(gas),}$$

so that the equilibrium Ce valence will be a function of pO_2 and *T*. Both in solids as in melts, for a given pO_2 the equilibrium shifts toward the right on heating, which results in severe Ce

reduction at high temperatures, even in air.[13,35] We assume that the just crystallised material reflects the melt state at the crystallisation temperature, so that significantly reduced phases are expected to crystallise even in air.

2) Just after crystallization and down to temperatures of ≃ 1200 °C, both cations and anions are highly mobile and phases with variable cation disorder and oxidation degree will form, their appearance and spatial distribution depending on the pO_2 of the chamber and oxygen diffusion rates within the solid.

For very low pO_2, as in the HLFZ case, the melt will solidify as *p*-$Ce_2Zr_2O_7$. For moderate or high pO_2, inward radial penetration of oxygen will occur, leading to oxidised phases whose disorder degree and spatial distribution will depend on pO_2, the cooling rates and the temperature dependence of the oxygen diffusion coefficients. The appearance of only cation-disordered phases when processing in air implies that oxygen reaches the rod centre at temperatures high enough to stabilise the DF phase. In the intermediate PLFZ case, the oxygen content reaching the centre is too low to stabilise disordered phases and the rod centre remains *p*-like, whereas near the surface the oxygen concentration is high enough to produce the DF phase. It is in this stage that the separation between pyrochlore and fluorite-like phases occurs, with the intermediate of partially reduced δ regions.

3) For temperatures below those enabling cation mobility oxidation events may still occur but will not change the cation distribution or very slowly. In this regime, under increasing oxygen content $Ce_2Zr_2O_7$ evolves first to an oxidised pyrochlore and then to β- phase, whereas DF evolves to *t*'-phase at the oxygen rich surface. The regions of reduced δ-phase will convert to a more oxidised state while keeping their partial cation order. The phase content of the samples studied in this work is summarised in Table 2. We include the results for the TG residuals (presented in the Supporting Information) to highlight that the order degree is not modified up

to 800 °C in air: *p* and β phases evolve to a common κ-phase, the DF phase transforms into the *t*'-phase and the δ-phase retains its partially ordered character.

Electronic Raman transitions among the crystal field split levels of Ce^{3+} ions have been discussed and assigned. The mapping of the $^2F_{5/2} \rightarrow {}^2F_{7/2}$ intermultiplet spectrum evidences a shift of the main band from ≈ 2100 up to ≈ 2150 cm^{-1} on going from DF or *t*'-phases to β or *p*-phases, which is attributed to differences in the Ce^{3+} local environment. The similar band position in the *p* and β phases suggests that the extra oxygen ions introduced in the β-phase do not affect largely the cerium environment. This hypothesis is supported by crystallographic data.[36] These show that the additional oxygen ions occupy the anionic vacancies of the *p* structure, which are closer to the Zr^{4+} cations than to the rare earth. To deepen into this point, we collect in Table 3 the band position in the different phases found in this work, together with the Ce site symmetry and average bond distances taken from the literature. As expected, average bond distances decrease gradually with increasing oxidation but the position of the main Ce^{3+} band does not present such a gradual evolution. This apparent discrepancy may have two contributions: the first one is that in partially oxidised phases the local relaxation around each individual Ce^{3+} ion results in longer Ce^{3+}-O bond distances compared to the average ones. The second contribution may come from the site symmetry change from trigonal to tetragonal-like upon going from ordered to disordered phases, which may result in different crystal-field splitting of the $^2F_{5/2}$ and $^2F_{7/2}$ multiplets.

5| SUMMARY AND CONCLUSIONS

Rods of nominal $Ce_{0.5}Zr_{0.5}O_2$ composition have been processed from the melt by LFZ either in an oxidising (air) or in a reducing (Ar + 5%H_2) atmosphere. Phase content and stoichiometry have been analysed by XRD, Raman spectroscopy, SEM, EDX, EBSD and TGA. Space-resolved

phase identification by Raman mapping, in particular, has been crucial to draw the phase landscape as a function of the cation-order degree and oxygen content.

The Raman spectra of defect fluorite, t', pyrochlore, β, δ and κ phases of CZO have been identified, clarifying some ambiguity in the existing literature. Pyrochlore, β and κ spectra show clearly distinct spectral features implying that, although these phases are structurally related, they belong to unambiguously different crystalline structures. An intermediate state between the pyrochlore and fluorite phases has been identified and named as δ-phase. We propose that it may consist of cation-ordered nuclei surrounded by disordered regions, analogous to the "κ-like" phases obtained by reoxidation of CZO samples previously submitted to reduction treatments at temperatures of the order of 1050-1100 °C.[10] The occurrence of such an intermediate state in the landscape of CZO phases may be relevant to understand the complex TPR behaviour because the reduction temperatures achieved in TPR experiments are usually below but close to 1000 °C, which may favour the development of the δ-phase.[5,25] The shift of the electronic Raman spectrum of Ce^{3+} ions is found to be a sensitive probe of the degree of cation order in CZO compounds.

ACKNOWLEDGEMENTS

The authors acknowledge the financial support from the Spanish Ministerio de Economía y Competitividad and Feder Funds under project MAT2016-77769-R. We thank the Servicio General de Apoyo a la Investigación-SAI (Universidad de Zaragoza) for technical support in X-ray diffraction and electron microscopy experiments. We also thank Rubén Gotor for technical assistance in sample preparation.

Supplementary Material is available, containing XRD profile fits of the processed materials, TG results, EDX analyses, additional SEM images, additional Raman spectra of the processed rods and after TGA, and EBSD analysis of the HLFZ and PLFZ samples.

References

[1] A. Trovarelli, P. Fornasiero (Eds), *Catalysis by ceria and related materials*, 2nd edition, Catalytic science series, vol. 12. Imperial College Press, London, **2013**.

[2] D. Devaiah, L. H. Reddy, S.-E. Park, B. M. Reddy, *Catalysis Reviews-Science and Engineering* **2018**, *60*, 177.

[3] P. Li, X. Chen, Y. Li, J. W. Schwank, *Catalysis Today* **2019**, *327*, 90.

[4] P. Fornasiero, R. di Monte, G. R. Rao, J. Kaspar, S. Meriani, A. Trovarelli, M. Graziani, *J. Catal.* **1995**, *151*, 168.

[5] I. Alessandri, M. A. Bañares, L. E. Depero, M. Ferroni, P. Fornasiero, F. C. Gennari, N. Hickey, M. V. Martinez-Huerta, T. Montini, *Top. Catal.* **2006**, *41*, 35.

[6] M. Yashima, K. Morimoto, N. Ishizawa, M. Yoshimura, *J. Am. Ceram. Soc.* **1993**, *76*, 2865.

[7] T. Negas, R. S. Roth, C. L. McDaniel, H. S. Parker, C. D. Olson, in *Proc. 12th Rare Earth Res. Conf.*, Vol. 2, (Ed: C. E. Lundin), University of Denver, Denver, Colorado, **1976**, pp. 605.

[8] M. Yashima, K. Morimoto, N. Ishizawa, M. Yoshimura, *J. Am. Ceram. Soc.* **1993**, *76*, 1745.

[9] M. L. Sanjuán, P. B. Oliete, A. Várez, J. Sanz, *J. Eur. Ceram. Soc.* **2012**, *32*, 689.

[10] T. Omata, H. Kishimoto, S. Otsuka-Yao-Matsuo, N. Ohtori, N. Umesaki, *J. Solid State Chem.* **1999**, *147*, 573.

[11] T. Sasaki, Y. Ukyo, A. Suda, M. Sugiura, K. Kuroda, S. Arai, H. Saka, *J. Ceram. Soc. Jpn.* **2003**, *111*, 382.

[12] S. N. Achary, S. K. Sali, N. K. Kulkarni, P. S. R. Krishna, A. B. Shinde, A. K. Tyagi, *Chem. Mater.* **2009**, *21*, 5848.

[13] B. Bulfin, A. J. Lowe, K. A. Keogh, B. E. Murphy, O. Lübben, S. A. Krasnikov, I. V. Shvets, *J. Phys. Chem. C* **2013**, *117*, 24129.

[14] B. Bulfin, F. Call, J. Vieten, M. Roeb, C. Sattler, I. V. Shvets, *J. Phys. Chem. C* **2016**, *120*, 2027.

[15] S. Urban, I. Djerdj, P. Dolcet, L. Chen, M. Möller, O. Khalid, H. Camuka, R. Ellinghaus, C. Li, S. Gross, P. J. Klar, B. Smarsly, H. Over, *Chem. Mater.* **2017**, *29*, 9218.

[16] G. Gouadec, P. Colomban, *Prog. Cryst. Growth Charact. Mater.* **2007**, *53*, 1.

[17] Bin Gao, T. Chen, D. W. Tam, C.-L. Huang, K. Sasmal, D. T. Adroja, F. Ye, H. Cao, G. Sala, M. B. Stone, C. Baines, J. A. T. Verezhak, H. Hu, J.-H. Chung, X. Xu, S.-W. Cheong, M. Nallaiyan, S. Spagna, M. B. Maple, A. H. Nevidomskyy, E. Morosan, G. Chen, P. Dai, *Nat. Phys.* **2019**, *15*, 1052.

[18] J. Gaudet, E. M. Smith, J. Dudemaine, J. Beare, C. R. C. Buhariwalla, N. P. Butch, M. B. Stone, A. I. Kolesnikov, Guangyong Xu, D. R. Yahne, K. A. Ross, C. A. Marjerrison, J. D. Garrett, G. M. Luke, A. D. Bianchi, B. D. Gaulin, *Phys. Rev. Lett.* **2019**, *122*, 187201.

[19] A. Várez, E. García-González, J. Jolly, J. Sanz, *J. Eur. Ceram. Soc.* **2007**, *27*, 3677.

[20] M. L. Sanjuán, P. B. Oliete, A. Várez, J. Sanz, *Bol. Soc. Esp. Ceram. Vidrio* **2008**, *47*, 165.

[21] V. M. Orera, R. I. Merino, J. I. Peña, *Solid State Ionics* **1994**, *72*, 224.

[22] T. Kasano, T. Arima, K. Idemitsu, Y. Inagaki, *Prog. Nucl. Energy* **2014**, *72*, 134.

[23] L. Kong, I. Karatchevtseva, D. J. Gregg, M. G. Blackford, R. Holmes, G. Triani, *J. Eur. Ceram. Soc.* **2013**, *33*, 3273.

[24] X. Zhang, X. Fang, X. Feng, X. Li, W. Liu, X. Xu, N. Zhang, Z. Gao, X. Wang, W. Zhou, *Catal. Sci. Technol.* **2017**, *7*, 2729.
[25] S. Otsuka-Yao-Matsuo, T. Omata, N. Izu, H. Kishimoto, *J. Solid State Chem.* **1998**, *138*, 47.
[26] T. Masui, Y. Peng, K.-I. Machida, G.-Y. Adachi, *Chem. Mater.* **1998**, *10*, 4005.
[27] D. L. Rousseau, R. P. Baumann, S. P.S. Porto, *J. Raman Spectrosc.* **1981**, *10*, 253.
[28] S. Nandi, Y.M. Jana, H.C. Gupta, *J. Phys. Chem. Solids.* **2018**, *115*, 347.
[29] M. Maczka, M. L. Sanjuán, A. F. Fuentes, L. Macalik, J. Hanuza, K. Matsuhira, Z. Hiroi, *Phys. Rev. B* **2009**, *79*, 214437.
[30] M. A. Subramanian, G. Aravamudan, G. V. Subba Rao, *Prog. Solid State Chem.* **1983**, *15*, 55.
[31] A. F. Fuentes, S. M. Montemayor, M. Maczka, M. Lang, R. C. Ewing, U. Amador, *Inorg. Chem.* **2018**, *57*, 12093.
[32] D. Michel, M. Perez y Jorba, R. Collongues, *Mat. Res. Bull.* **1974**, *9*, 1457.
[33] T. Moriga, A. Yoshiasa, F. Kanamaru, K. Koto , M. Yoshimura, S. Somiya, *Solid State lonics* **1989**, *31*, 319.
[34] H. D. Schreiber, S. J. Kozak, K. K. McManus, Lunar and Planetary science XVII, **1986**, 773.
[35] D. J. Smythe, J. M. Brenan, *Geochim. Cosmochim. Acta* **2015** *170*, 173.
[36] T. Sasaki, Y. Ukyo, K. Kuroda, S. Arai, S. Muto, H. Saka, *J. Ceram. Soc. Jpn.* **2004**, *112*, 440.

TABLE 1 Wavenumbers of the bands observed in the Raman spectrum of $Ce_2Zr_2O_7$ at RT and 77 K below 3000 cm^{-1}. The last column gives the attribution based on polarisation measurements.

Raman shifts/cm^{-1} at RT	Raman shifts/cm^{-1} at 77K	Attribution
294	300	T_{2g}
301	306	E_g
372	375	unassigned
392	398	T_{2g}
448	446	T_{2g}
	455	Intra $^2F_{5/2}$ CF transition
497	500	A_{1g}
527	528	T_{2g}
587	596	Second order excitation or extra oxygen in vacant site
720	730	Vibronic (CF + phonon)
809	811	Vibronic (CF + phonon)
892	888	Intra $^2F_{5/2}$ CF transition
2147	2144	$^2F_{5/2} \rightarrow {}^2F_{7/2}$ CF transition
2492	2497	$^2F_{5/2} \rightarrow {}^2F_{7/2}$ CF transition
2556	2551	$^2F_{5/2} \rightarrow {}^2F_{7/2}$ CF transition
2757	2750	$^2F_{5/2} \rightarrow {}^2F_{7/2}$ CF transition

TABLE 2 Phase content of the samples studied in this work. The average stoichiometry is derived from TG experiments.

Label	Processing atmosphere	Average stoichiometry	As-processed, core	As-processed, outer region	After TG at 800 °C in air
ALFZ	air	$Ce_{0.43}Zr_{0.57}O_{1.97}$	DF	*t*′	*t*′
PLFZ	intermediate pO_2	$Ce_2Zr_2O_{7.56}$	*p*, β	δ, DF, *t*′	κ, δ, *t*′
HLFZ	Ar + 5% H_2	$Ce_2Zr_2O_{7.28}$	*p*	β	κ

TABLE 3 Crystallography of the Ce site and electronic Raman shift of the main $^2F_{5/2} \rightarrow {}^2F_{7/2}$ transition.

Phase	SG	Ce site symmetry	Ce-O bond distances (Å)	Ce^{3+} Raman shift/cm^{-1}
t'- $Ce_{0.5}Zr_{0.5}O_{2-\delta}$	$P4_2/nmc$	2*a* (D_{2d})	4x2.18, 4x2.41[19]	2105±2
DF - $Ce_{0.5}Zr_{0.5}O_{2-\delta}$	$Fm\bar{3}m$	4*a* (O_h)	8x2.29[8]	2104±2
δ - $Ce_2Zr_2O_{7+z}$	?			2130±2
β - $Ce_2Zr_2O_{7+z}$	$F\bar{4}3m$	16*e* (C_{3v})	3x2.44, 3x2.58, 2.27, 2.34[36]	2144±2
p - $Ce_2Zr_2O_7$	$Fd\bar{3}m$	16*c* (D_{3d})	6x2.61, 2x2.33[36]	2143±2

Figure Captions

FIG. 1 (a) SEM image of a transverse section of the ALFZ processed rod and (b) Raman spectra of the ALFZ sample recorded at the rod centre (in red) or near the edge (in blue), attributed to a defect fluorite and *t*' phases, respectively. The inset shows the Ce^{3+} electronic Raman spectrum measured at the rod centre. The laser wavelength is 496.5 nm.

FIG. 2 XRD patterns of CZO samples: (a) ALFZ, processed in air; (b) HLFZ, processed in Ar + 5%H_2; (c) PLFZ, processed in $pO_2 \simeq 0.01$ bar. The upper inset shows a magnification of the 36.5° region of pattern (c), to highlight the double-peak aspect of superstructure reflections denoting cation ordering. The inset on the right shows the high angle peaks of the HLFZ pattern to put into evidence the presence of a minor amount of a second phase.

FIG. 3 Portion of the transverse section of the HLFZ sample (left) and selected Raman spectra recorded at RT onto different points of the sample (right). The laser wavelength is 496.5 nm.

FIG. 4 (a) XRD patterns of $Ce_2Zr_2O_{7.3}$ (N7.3, lower graph) and $Ce_2Zr_2O_{7.5}$ (N7.5, upper graph) reference samples. The inset shows the presence of the (200) reflection in both samples, denoting $F\bar{4}3m$ SG, together with the (111) pyrochlore superstructure peak. (b) The RT Raman spectra of $Ce_2Zr_2O_{7.3}$ (middle spectrum) and $Ce_2Zr_2O_{7.5}$ (lower spectrum) reference samples are compared to the problem spectrum (upper graph) found close to the pyrochlore phase in HLFZ and PLFZ samples (see spectra 3(c) and 5(b)). The laser wavelength is 496.5 nm.

FIG. 5 Optical microscope picture of a transverse section of a PLFZ rod and Raman spectra recorded at RT in different points of the surface. Spectra assignment is (see text): (a) Slightly oxidised pyrochlore, (b) β-phase, (c) δ-phase, (d) defect-fluorite and (e) *t*'-phase. Spectrum (e) displays some contribution of the CeO_2 band at 465 cm^{-1}, in agreement with the presence of this phase at the rod surface. The laser wavelength is 496.5 nm.

FIG. 6 Raman spectra of $Ce_2Zr_2O_7$ recorded onto a (001) plane in (a) *z*(*xx*)-*z*, (b) *z*(*xy*)-*z*, (c) *z*(*x*'*x*')-*z* and (d) *z*(*x*'*y*')-*z* configurations, where *x*, *y* stand for [100] and [010] directions and *x*' and *y*' denote crystal directions at 45° from {*x*, *y*}. The left and right part of the figure display spectra recorded at RT and 77K, respectively. The inset in the left part highlights the presence of a band at 527 cm^{-1} with T_{2g} polarisation properties. The laser wavelength is 496.5 nm.

FIG. 7 Electronic Raman spectrum involving intermultiplet $^2F_{5/2} \rightarrow {}^2F_{7/2}$ transitions of Ce^{3+} ions in $Ce_2Zr_2O_7$, measured at 514.5 nm in configurations: (a) *x*'*y*', RT, (b) *x*'*x*', RT, (c) *x*'*y*', 77K, (d) *x*'*x*', 77K.

FIG. 8 RT Electronic Raman spectrum of Ce^{3+} ions involving intermultiplet $^2F_{5/2} \rightarrow {}^2F_{7/2}$ transitions in: (a) stoichiometric pyrochlore, (b) slightly oxidised pyrochlore, (c) β, (d) δ, and (e) *t'* CZO phases. The laser wavelength is 496.5 nm.

Figure 1

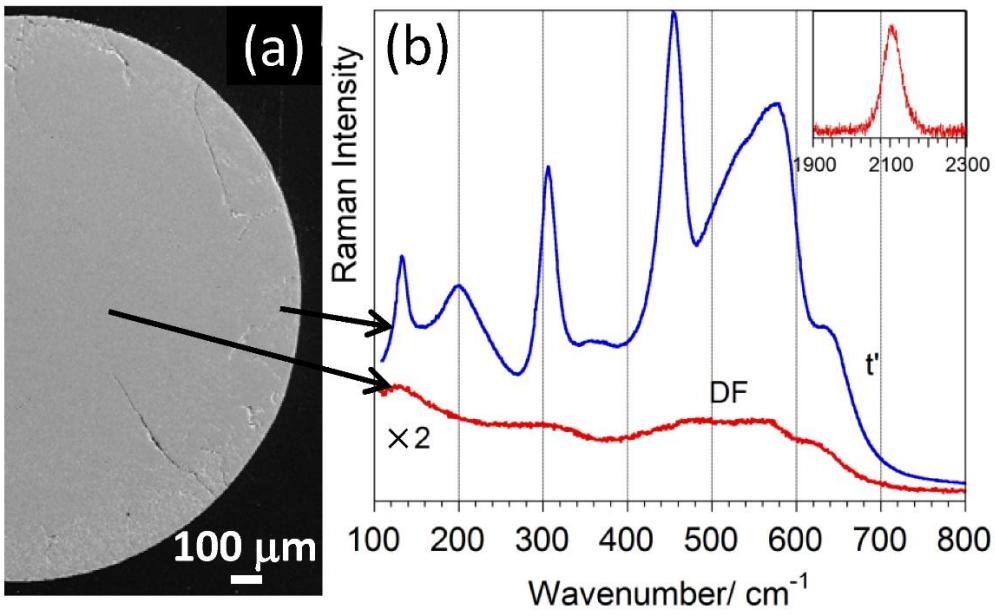
(a)
100 μm
(b)
Raman Intensity
1900
2100
2300
t'
DF
×2
100
200
300
400
500
600
700
800
Wavenumber/ cm-1

Figure 2

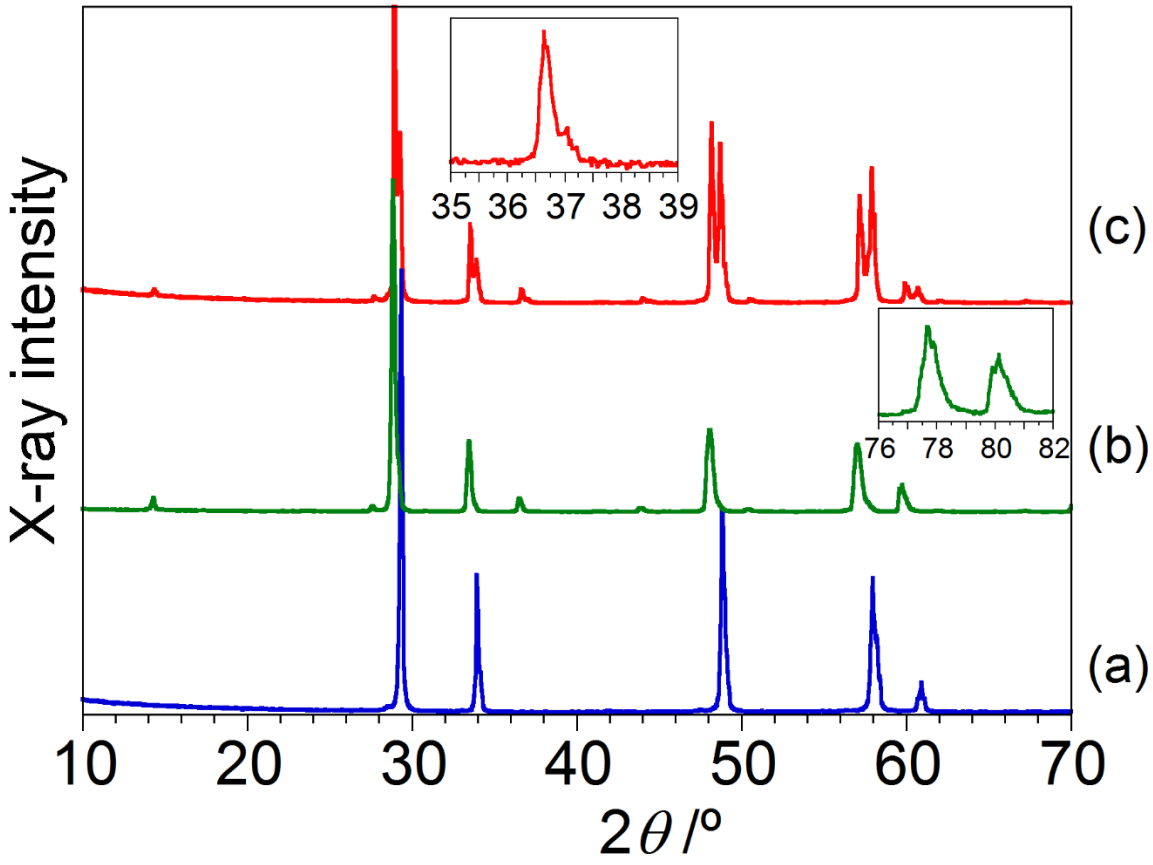
X-ray intensity
35 36 37 38 39
76 78 80 82
(c)
(b)
(a)
10 20 30 40 50 60 70
2θ /°

Figure 3

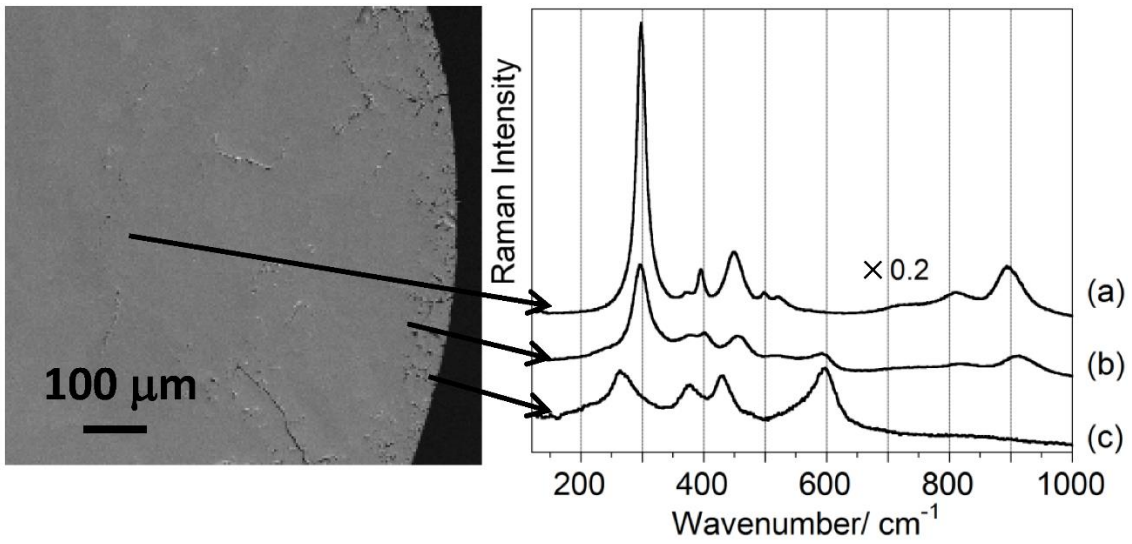
100 μm
Raman Intensity
×0.2
(a)
(b)
(c)
200
400
600
800
1000
Wavenumber/ cm-1

Figure 4

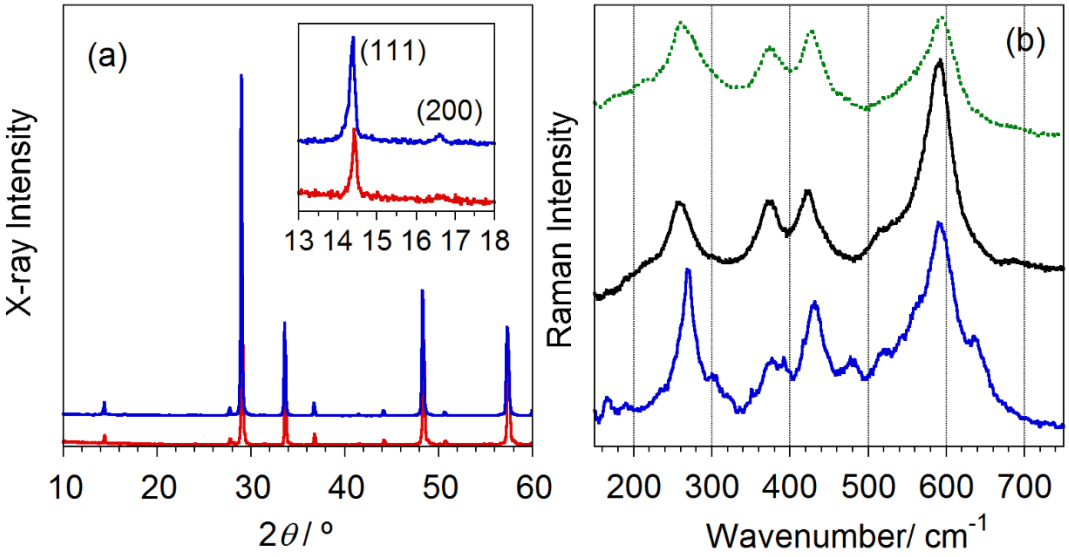
(a)
(111)
(200)
13 14 15 16 17 18
X-ray Intensity
10 20 30 40 50 60
2θ / °
(b)
Raman Intensity
200 300 400 500 600 700
Wavenumber/ cm-1

Figure 5

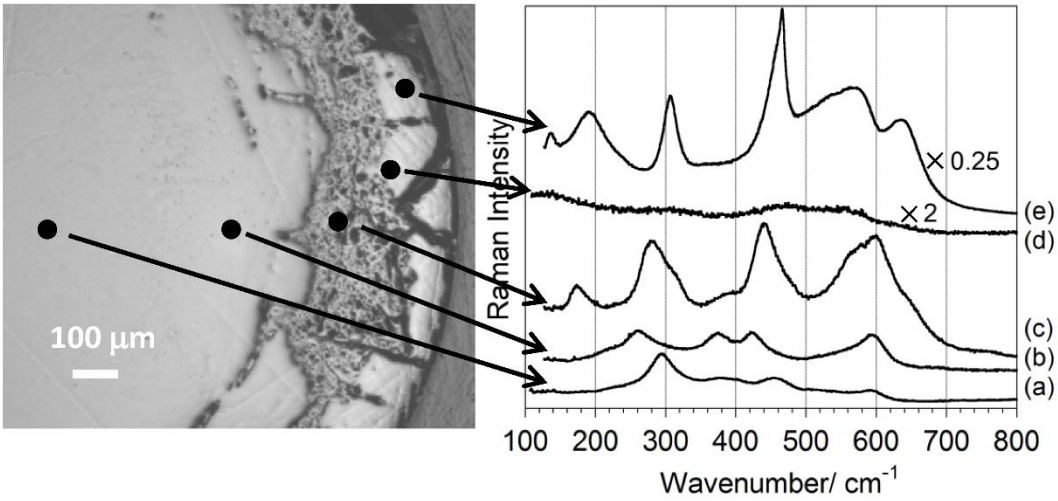
100 μm
Raman Intensity
× 0.25
× 2
(e)
(d)
(c)
(b)
(a)
100 200 300 400 500 600 700 800
Wavenumber/ cm-1

Figure 6

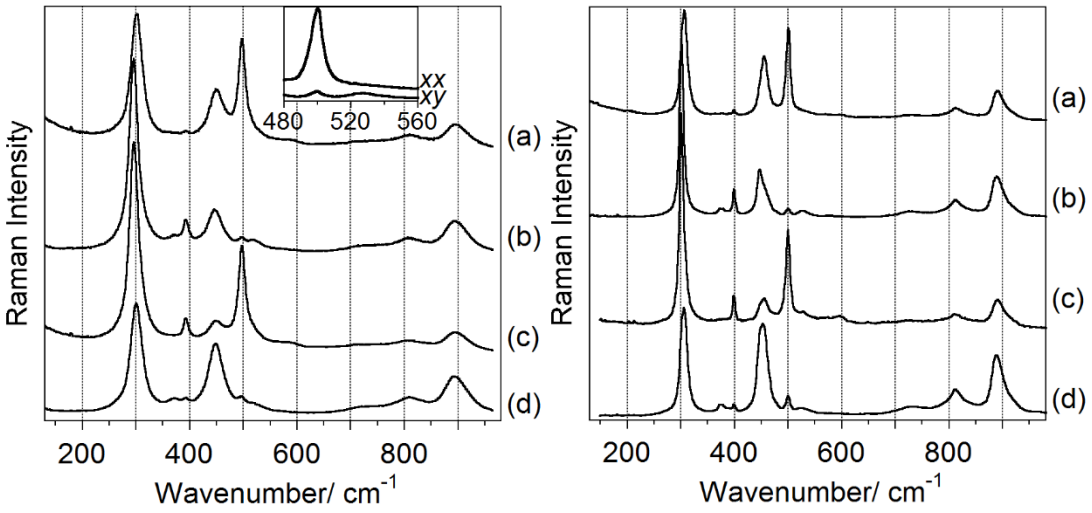
Raman Intensity
Wavenumber/ cm-1
200
400
600
800
480
520
560
xx
xy
(a)
(b)
(c)
(d)

Figure 7

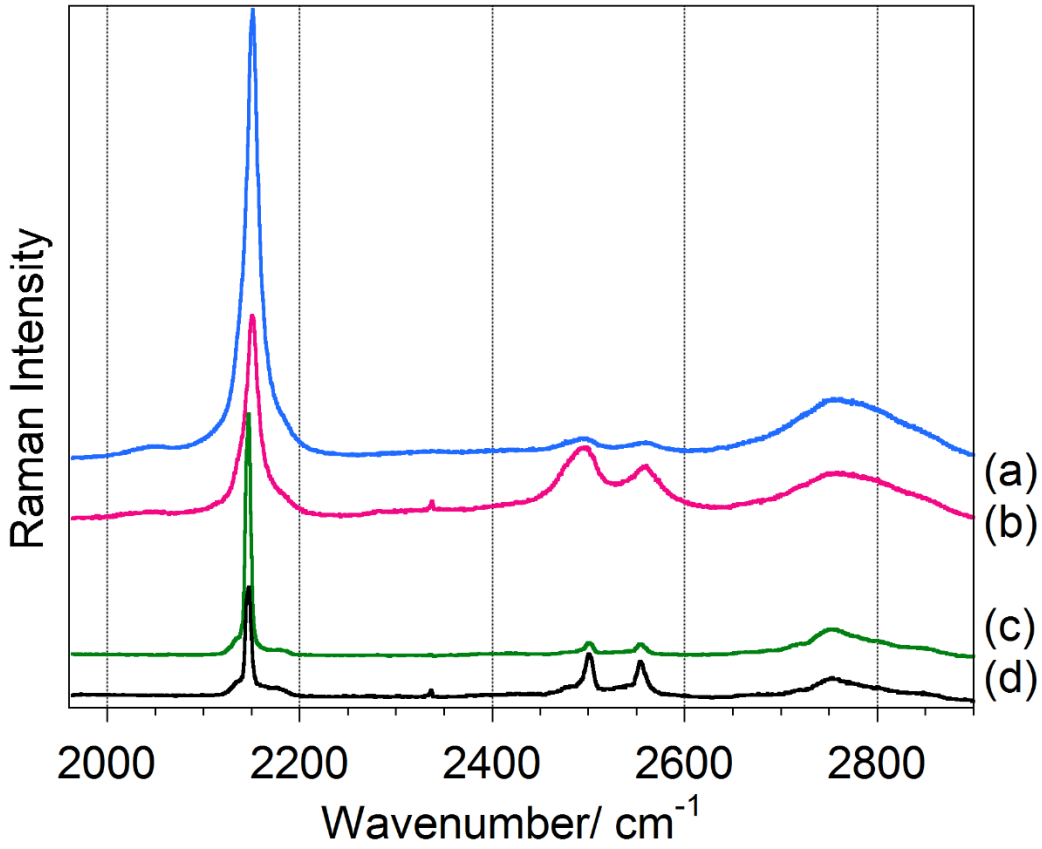
Raman Intensity
(a)
(b)
(c)
(d)
2000
2200
2400
2600
2800
Wavenumber/ cm-1

Figure 8

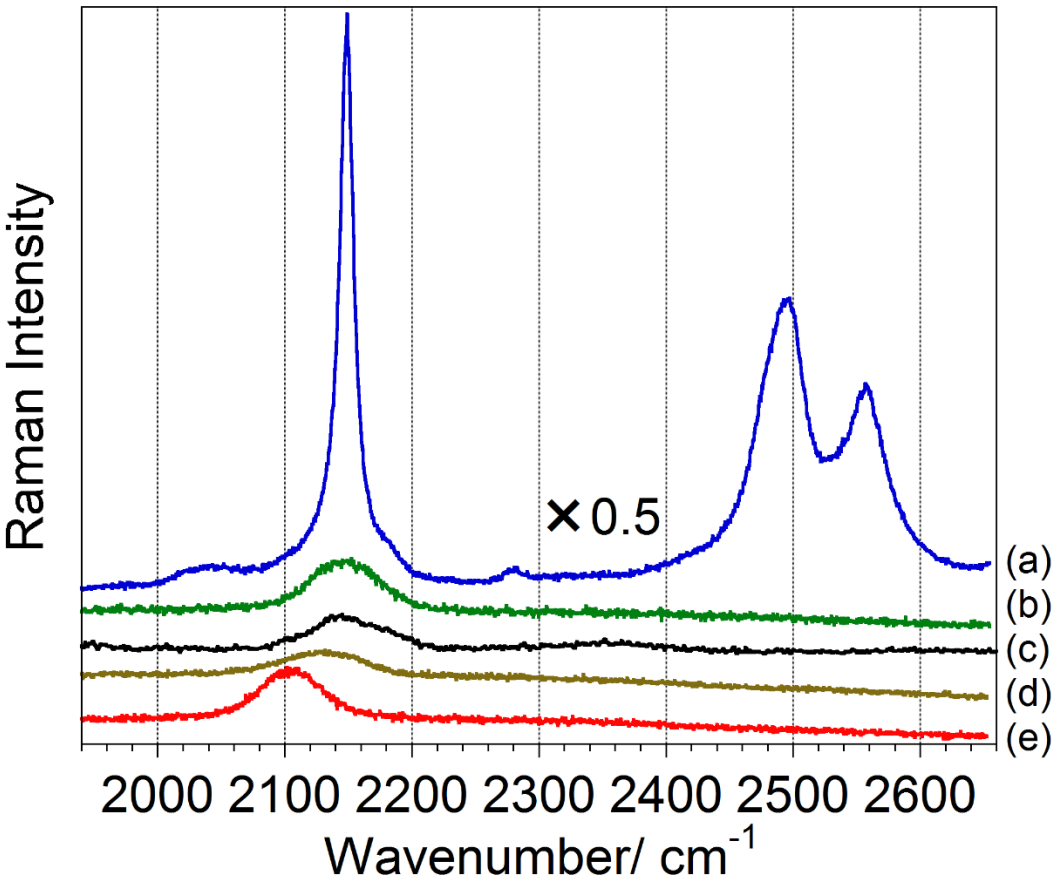
Raman Intensity
×0.5
(a)
(b)
(c)
(d)
(e)
2000 2100 2200 2300 2400 2500 2600
Wavenumber/ cm-1